JOURNALS | Journal of Visual Artificial Intelligence

Volume 2 Issue 2 (September 2026)
J. Vis. Artif. Intell., 2026, 1(2), 26107
DOI : https://doi.org/10.64189/vai.26107

Research Article

OPEN ACCESS

Q-MedDict: A Classical Quantum-Inspired Dictionary for Lung Tissue Images and Laboratory Metadata

Sazia Parvin* and Md Sarwar Kamal*

Melbourne Polytechnic Melbourne, VIC, 3072, Australia

*Corresponding Author
Sazia Parvin
SaziaParvin@melbournepolytechnic.edu.au
Md Sarwar Kamal
mdsarwarkamal@melbournepolytechnic.edu.au

Received: 08 August 2026
Revised: 16 September 2026
Accepted: 21 September 2026
Published Online: 22 September 2026

Citation

S. Parvin, M. S. Kamal, Q-MedDict: Quantum dictionary multimodality for lung tissue and lab data, *Journal of Visual Artificial Intelligence*, 2026, 1(2), 26107, https://doi.org/10.64189/vai.26107.

Open Access

This article is licensed under a Creative Commons Attribution-NonCommercial 4.0 International License, which permits the non-commercial use, sharing, adaptation, distribution and reproduction in any medium or format, as long as appropriate credit to the original author(s) and the source is given by providing a link to the Creative Commons License and changes need to be indicated if there are any. The images or other third-party material in this article are included in the article's Creative Commons License, unless indicated otherwise in a credit line to the material. If material is not included in the article's Creative Commons License and your intended use is not permitted by statutory regulation or exceeds the permitted use, you will need to obtain permission directly from the copyright holder. To view a copy of this License, visit: https://creativecommons.org/licenses/by-nc/4.0/

© The Author(s) 2026

Abstract

In the age of the information superhighway, artificial intelligence is assisting in health care and other medical domains. Considering the usefulness of AI, it would be beneficial to have automated lung cancer identification based on various cancer data. These data could be images, tabular data, or handwritten notes. Lung cancer data may include images and laboratory findings, and may have different structures and scopes. In this research, we present a classical quantum-based dictionary representation to handle various combinations of data. The quantum dictionary facilitates the superposition principle of quantum computing. It does not run on quantum hardware but is instead considered as a logical representation of a quantum dictionary using superposition. We have used dictionary framework with quantum gates such as H, S, T, CX, and CCX with matrix formation. Moreover, we utilize discrete cosine transform (DCT) and Karhunen–Loève transform (KLT) image sources. We found that our proposed approach shows better performance at 25% coefficient value improvements. Moreover, quantum dictionary-based key and value pairs ensure Hadamard-centric image formations up to 30.85 dB and 24.34 dB peak signal-to-noise ratio (PSNR). Similarly, proposed approach performs over other image sources like DCT up to 32.77 dB and 26.38 dB.

Keywords: Quantum-inspired dictionary; Classical simulation; Digital pathology; Lung H&E, Laboratory metadata; NHANES; Hadamard transform; Multimodal representation.

1. Introduction

Explainable artificial intelligence (XAI) and quantum computing (QC) offer beneficial advantages in cancer data analytics.[1] Data of disease such as cancer data can include various data types. This data can be XRAY, images, laboratory sample findings, practisioner notes and text.[2] A pathologist can look at a slide of stained tissue. A doctor can also look at your blood and urine tests. Such combinations of data are known as multimodal data. These data don't seem to be alike. An image can be made of millions of pixels. A laboratory table can only have a few values. Thus, a multimodal system needs to be able to make the source of each value visible.[3] Multimodal data analytics would provide insights about insights about cancer disease.[4] One of the key initialization is process data digitally. In such, digital pathology is growing quickly for medical data analytics. In this case, XAI and QC would be effective to handle large amount of data.[5]

Recent lung pathology models can read many tissue patterns from images. Other work moves toward multimodal pathology. MuPD places histology, RNA, and text in a shared space.[6] H_2O integrates Hematoxylin and Eosin (H& E) stained tissue images with spatial multi-omics data.[7] SpatialFusion combines tissue, expression, and pathway information.[8] These models use learned representations and large training sets. There is also growing interest in quantum computing and its applications in medical data analysis.[9] Quantum image representation methods, such as Flexible Representation of Quantum Images (FRQI) and Novel Enhanced Quantum Representation (NEQR), encode image information into quantum states.[10,11] The Quantum Pixel Representation (QPIXL) framework was used to support quantum image analysis and manage circuit data.[12] From the study, we see that our proposed approach and these approaches are not same. We find a few research gaps in the existing literature. These gaps are related to processing multimodal data using a classical model, the black-box nature of the models, and the lack of interpretability.[13] Black-box models are those that perform their operations through a large number of iterations, making it difficult to understand and track how the operations are concluded.[14,15] In this case, we only get the output, not an understanding of how it was obtained. However, in medical research, not all experts have an AI background. Therefore, we need interpretable AI models.[16] Similarly, there are some other gaps related to the complexities of quantum computing interactions. To avoid quantum complexities, we introduce dictionary-based quantum computing for processing larger datasets as well as improving interpretability. The public sources are important. Cancer Moonshot Biobank–Lung Cancer Collection (CMB-LCA) is a Cancer Moonshot Biobank lung cancer collection hosted by The Cancer Imaging Archive (TCIA) and represented in Imaging Data Commons (IDC).[17,18] The National Health and Nutrition Examination Survey (NHANES) is a separate public survey. Its Complete Blood Count (CBC) file includes WBC, haemoglobin, and platelet measures.[19] Its biochemistry file includes albumin, BUN, creatinine, and glucose.[20] Its urine file includes urine albumin, urine creatinine, and albumin-tocreatinine ratio.[21] In this research we have the following contributions:

1) A classical quantum-centric dictionary with explicit bitstring keys and amplitudes.
2) A direct numerical demonstration of all five stated dictionary rules: H, S, T, CX, and CCX.
3) A lung H&E block experiment with Hadamard, DCT, and PCA/KLT references. To prove the hypothesis, we consider a research question, which is: Can a classical quantum-based dictionary form design lung cancer image and pathological metadata in a reliable way, while considering sparse representation to be calculated separately?

2. Related work

Cancer image may contain small cell details and large tissue regions (Fig. 1). A workflow is to cut the slide into tiles. Each tile is translated into features. CLAM used attention-based multiple instance learning for weakly supervised image analysis.[22] Current foundation models are trained on larger collections of pathology. PulmoFoundation focuses on lung pathology.[23] Foundation models for pathology also suffer from issues like stain variation, site variation, data size, and clinical Validation.[24] Here these problems are critical because two demonstration images cannot show the entire range of lung pathology. MuPD integrates histology, RNA and text.[25] H_2O and SpatialFusion bridge tissue with molecular data.[26,27] OmiCLIP connects histology and spatial transcriptomics.[7] These methods utilize funcitons centric data and find hidden imag spaces. Q-MedDict is dictionary-based approach. In this method, combines a specific image pixel with respect to a desired location which is a key. Each key can show a modality and a feature position. So, our proposed method is a lightweight model that performs well on multimodal data within quantum scopes. In particular, the quantum features with superposition make it a strong candidate for handling multimodal data in cancer data analysis. FRQI stores image colour information in probability amplitudes and image position in basis states.[28] NEQR stores grayscale values in computational basis states.[29] QPIXL provides a common circuit framework for several quantum pixel representations.[30] These approaches are regular quantum-state representations or circuit foundations. One the other hand, our proposed Q-MedDict is different as this is dictionary-based data mapping. It is a classical dictionary-based data structure

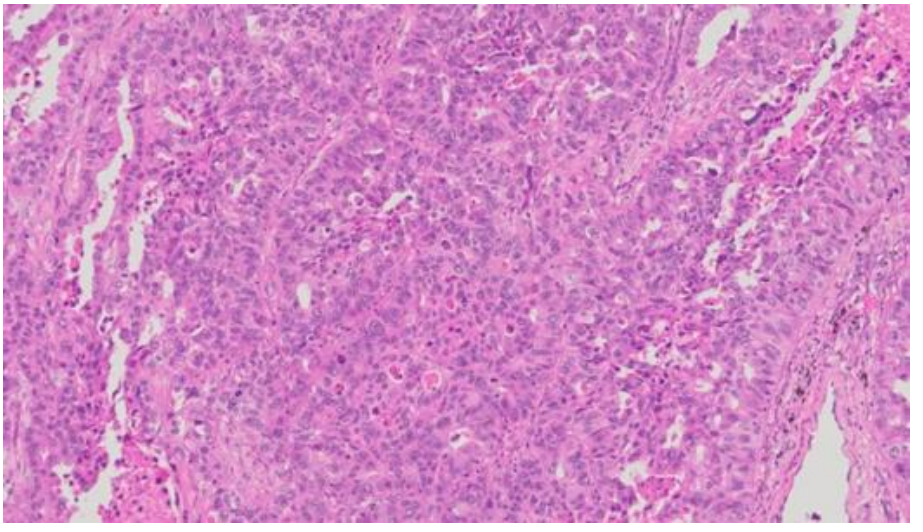


Fig. 1: Lung adenocarcinoma image.

using quantum notation. In this approach, we do not need a quantum processor. The data orientations are dictionary keys and values pair. The quantum gate functions rules are general deterministic update functions. According to the a newly proposed method, image color values data are Image color information is stored in probability amplitudes.[31] Similarly, a grayscale values are stored in computational basis states.[32] Another research find out a generic circuit structure for many quantum pixel representations is provided by QPIXL.[12] Our proposed method QMedDict is not the same. It is a traditional data format that draws inspiration from quantum notation. The bit strings are standard dictionary keys.

2.1 Positioning against baselines

Table 1 presents the descriptions of existing approaches and our proposed approach. DCT works on image transform. Other methods such as PCA/KLT is a data-centric linear transform. On the other hand, FRQI and NEQR are quantum image representations. Our proposed, Q-MedDict offer key and value combinaitons to trace each data with their locations.

3. Data and study design

In this research, we used publicly available data. One of the data is CMB-LCA is a public lung cancer collection from the Cancer Moonshot Biobank. All these data.[17] IDC lists slide microscopy as one of its modalities.[18]

3.1 NHANES blood and urine data

We have collected the laboratory data from public NHANES documentation for the August 2021 to August 2023 release. Table 2 presents the summaries of the metadata we used in this research from laboratory data. These are:

• CBC_L: WBC, haemoglobin, platelet count and other blood-cell measures.

• BIOPRO_L: albumin, BUN, serum creatinine, glucose and other chemistry measures.

• ALB_CR_L: urine albumin, urine creatinine, and albumin/ creatinine ratio.

4. Q-Meddict method

Our proposed method is an integrated approach of multiple processes. The proposed framework shown in Fig. 2. In this figure we see that, first step is about data collections and then normalizations and so on until the last state which is re-building the image. A state is stored as

$$S = \{(b_i, a_i) \mid b_i \in \{0,1\}^n, a_i \in \mathbb{R} \; or \; \mathbb{C} \tag{1}$$

The key b_i is a bit sequence. The amplitude a_i present the amount connected to that key. For an image patch, a key can show a pixel location. For a table, a key can mark a feature slot. In Table 3, we present quantum dictionary-based gates and rules which account for quantum data processing.

The amplitudes are presented by

$$a_i' = \frac{a_i}{\sqrt{\left(\sum_j |a_j|^2\right)}}, \tag{2}$$

which gives

$$\sum_i |a_i'|^2 = 1 \tag{3}$$

4.1 Image branch

Each lung H&E image is presented to grayscale for the present value. The image is represented as a 256× 256 array and split into 16×16 blocks. A block contains 256 values.

For compact notation, the orthonormal Hadamard gate is

$$C = HBH^T, \tag{4}$$

where B is one image location and H is a normalised Hadamard table. The largest K are kept:

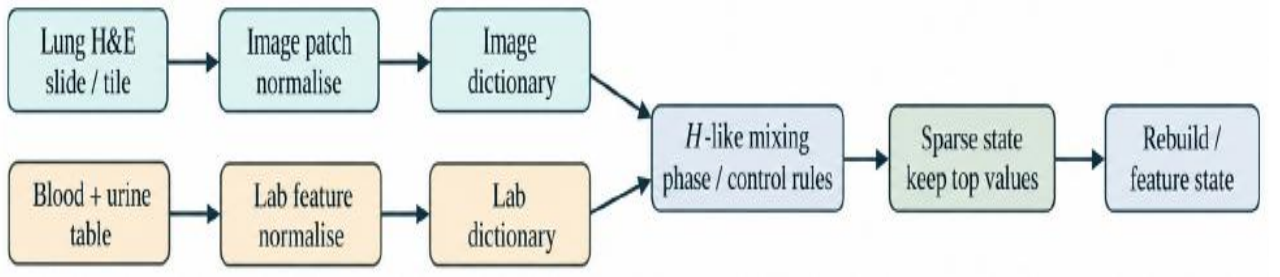


Fig. 2: Q-MedDict framework.

Table 1: Descriptions of various methods along with our proposed method

Approach	Data types	Methods	Advantages	Variations
DCT[33]	Graphical image data	Cosine similarity	Classical computing for image data	Modality based
PCA/KLT	Vector/image Segments	Geometrical structure	Linear formation	Gate based analysis
FRQI[28]	Image and graphical data	Quantum computing	Image on quantum state	Needed a quantum computing design
NEQR[29]	Image data	Gray scale image encoding	Grayscale basic design	Quantum image design
QPIXL[12]	Image data	Quantum pixel design	Quantum image circuit approach	Circuit based
Q-MedDict	Graphical image data and tabular lab data	Dictionary based design	Keys and values	A small representation analysis

Table 2: NHANES release metadata used in the laboratory branch. these are codebook ranges and counts, not patient measurements

Type	Variable	Public value range	Valid records	Availability
Blood	WBC (1000 cells/μL)	2.1–20.8	7,593	87.01%
Blood	Haemoglobin (g/dL)	6.3–18.6	7,593	87.01%
Blood	Platelets (1000 cells/μL)	46–787	7,593	87.01%
Blood	Serum albumin (g/dL)	2.2–5.5	6,366	88.43%
Blood	BUN (mg/dL)	4–74	6,326	87.87%
Blood	Serum creatinine (mg/dL)	0.33–15.17	6,326	87.87%
Blood	Serum glucose (mg/dL)	40–898	6,357	88.30%
Urine	Urine albumin (μg/mL)	0.01–7942.47	8,153	96.00%
Urine	Urine creatinine (mg/dL)	4–873	8,154	96.01%
Urine	Albumin/creatinine ratio (mg/g)	0–14708.28	8,153	96.00%

Table 3: Dictionary rules used for Q-MedDict

Rule	Simple role in the dictionary
H	Mix a pair of amplitudes as $(a_0 + a_1)/\sqrt{2}$ and $(a_0 - a_1)/\sqrt{2}$.
S	Multiply amplitudes whose target bit is 1 by i.
T	Multiply amplitudes whose target bit is 1 by $e^{i\pi/4}$.
CX	Flip a target key bit when one control key bit is 1.
CCX	Flip a target key bit when two control key bits are 1.

$$\tilde{C}_j = \begin{cases} C_j, & j \in \mathcal{K}, \\ 0, & \text{otherwise.} \end{cases} \quad (5)$$

The block is supported by

$$\tilde{B} = H^T \tilde{C} H. \quad (6)$$

We test K = 128, 64, and 32. These values keep 50%, 25%, and 12.5% of block coefficients.

Our proposed key and dictionary quantum approach support pairwise H gate update to key and value combinations. The matrix structure is used because it is easy to execute and get output. We verified dictionary values and the reference matrix output in Table 4. We also report the fraction of squared transform coefficients kept:

$$R_E = \frac{\sum_{j\in\mathcal{K}} |C_j|^2}{\sum_j |C_j|^2} \times 100. \quad (7)$$

Here we see that due to Hadamad gate H is orthonormal, the full energy before and after the transform is the same. Therefore, RE is not supporting that the transform "preserves energy." It measures how reserved the coefficients are after top-K selection.

4.2 Laboratory metadata branch

We define the experiments as follows:

$$r_i = \log\left(1 + \max_i - \min_i\right) \quad (8)$$

and a release completeness value

$$q_i = \frac{N_{valid,i}}{N_{total,i}}. \quad (9)$$

The reserved descriptor used $r_i q_i$ before min and max scaling and amplitude normalization.

Our interpretation as follows: where r_i and q_i are descriptors. We also do not recommend multiplying a future patient measurement by qi. We define a record is q_i. We define a record is

$$S_L = \{(b_i, a_i, m_i, q_i)\}, \quad (10)$$

where a_i is a scaled value, m_i is a missing value, and q_i is a metadata.

4.4 Gate-like dictionary rules

Q-MedDict uses classical update rules inspired from quantum computing rules.

5. Experimental setup

In these experiments we used two public lung adenocarcinoma images. Each image was divided into 256 groups of 16 × 16 pixels. Hadamard values were managed by true size. These are 128, 64, or 32. For a base line outcome, we used same arrays and the same top-K rule with a two-dimensional orthonormal DCT image. A PCA/KLT values was also used. For PCA/KLT, one image was used to the 512 blocks from the two demonstration images. The storage cost is not measured.

Table 5: Lung H&E image results for the Hadamard-gate

Image	Keep (%)	PSNR (dB)	SSIM	Energy (%)
H&E-1	50.0	37.60	0.983	99.96
H&E-1	25.0	30.85	0.919	99.80
H&E-1	12.5	27.47	0.814	99.56
H&E-2	50.0	31.24	0.978	99.87
H&E-2	25.0	24.34	0.910	99.35
H&E-2	12.5	20.83	0.809	98.58

Table 6: Image baselines at 64 of 256 coefficients per block (25%)

Image	Method	PSNR (dB)	SSIM	Image	Method
H&E-1	Hadamard	30.85	0.919	H&E-1	Hadamard
H&E-1	DCT	32.77	0.947	H&E-1	DCT
H&E-1	PCA/KLT	28.89	0.864	H&E-1	PCA/KLT
H&E-2	Hadamard	24.34	0.910	H&E-2	Hadamard
H&E-2	DCT	26.38	0.942	H&E-2	DCT
H&E-2	PCA/KLT	25.04	0.910	H&E-2	PCA/KLT

5.1 Laboratory metadata experiment

The NHANES instructions were utilized to record the minimum, maximum, valid count, and total count. Seven blood descriptors and three urine descriptors were also used. We also used "release-metadata framework." Moreover, we also added a numerical sensitivity check. It checks the initial $r_i q_i$ descriptor with: (i) weighting, (ii) no log transform, and (iii) identity top-K keeping.

5.2 Scope rule

We define the image and other metadata for our experimental analysis. We consider these data to investigate our hypothesis weather quantum dictionary-based model can have better utilization of superposition.

6. Results

6.1 Lung image encoding results

Table 5 presents the original Hadamard-gate centric image outcomes. Most values are representing the image data analysis with various combinations. Table 6 presents further outcomes of 25% baseline comparative analysis. The DCT is perform better outcomes in comparison with the Hadamard for PSNR and SSIM images. Similarly, the PCA/KLT is shows in between outcomes. QMedDict offers better scopes for dictionary representation and rule tracing. Fig. 3 shows grayscale image and its 25% Hadamard framework. The largest framework remains usable. Fig. 4 shows that PSNR falls when fewer coefficients are kept. The dictionary values

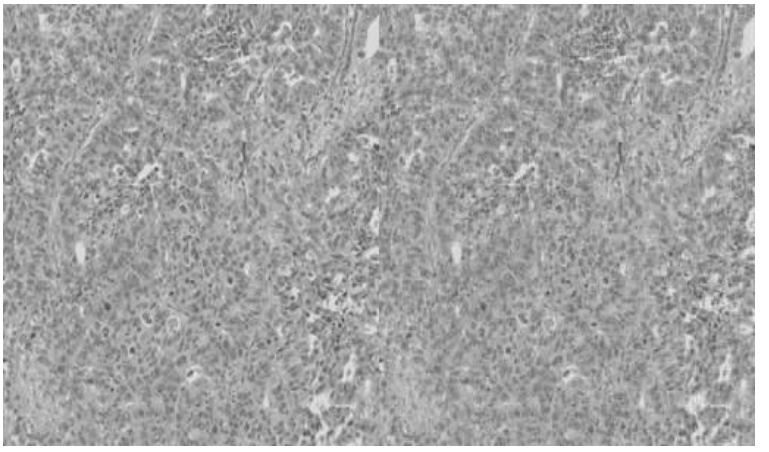


Fig. 3: Lung image which is rebuilt after keeping 64 of 256 Hadamard coefficients in each 16 × 16 block.

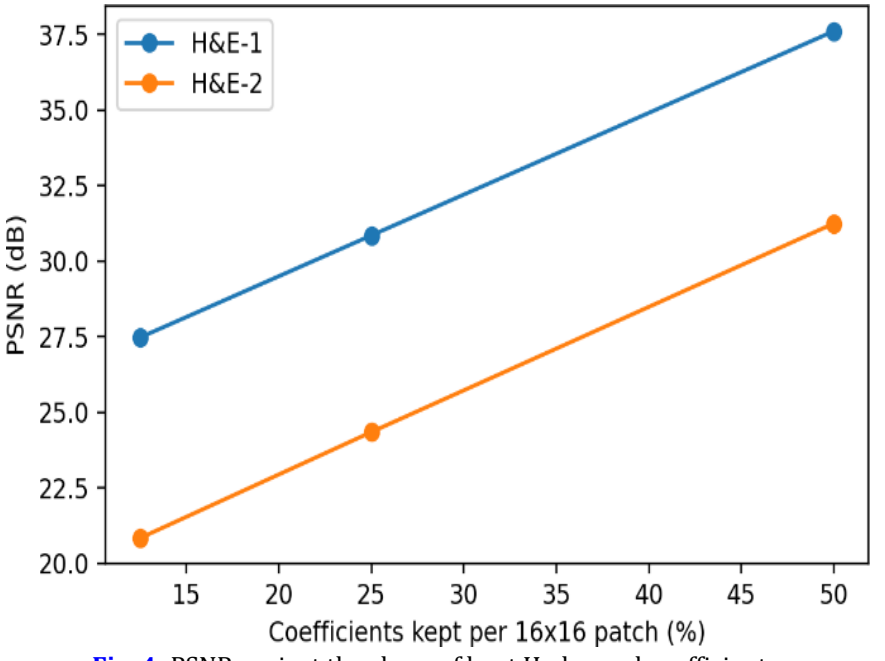


Fig. 4: PSNR against the share of kept Hadamard coefficients.

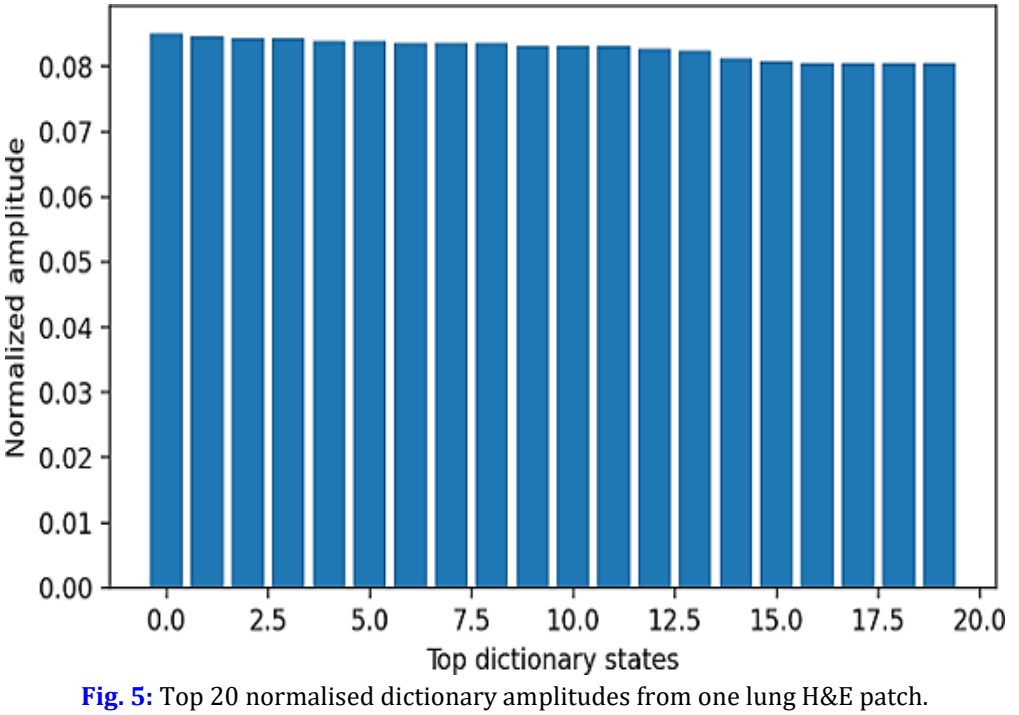


Fig. 5: Top 20 normalised dictionary amplitudes from one lung H&E patch.

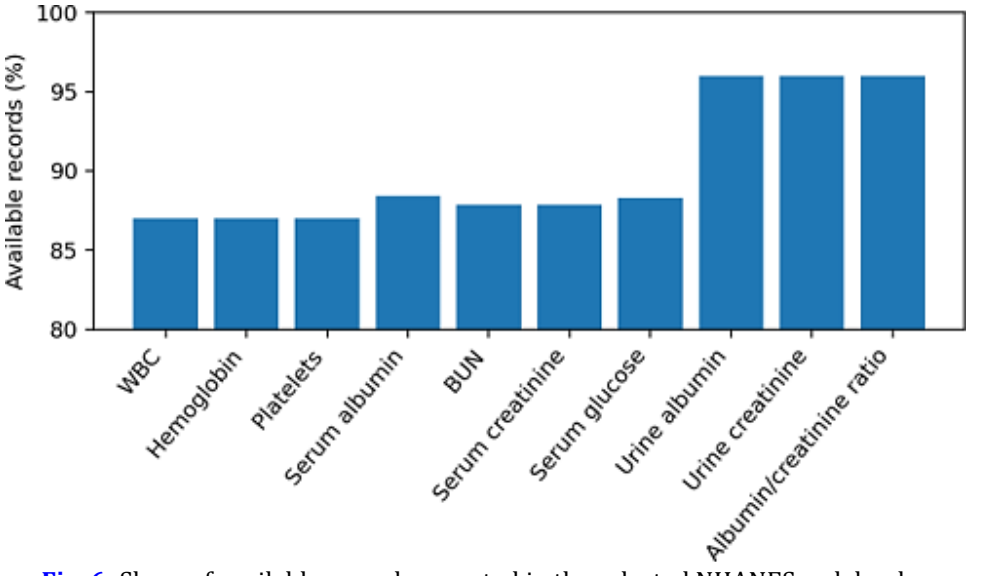


Fig. 6: Share of available records reported in the selected NHANES codebooks.

are irregular. Fig. 5 shows the 20 largest values from one tissue patch.

6.2 Blood release-metadata results

Fig. 6 shows the comparative outcomes for completeness values. Blood variables are around 87 to 88% complete in the selected files. Urine variables are around 96%. Table 7 presents descriptor reconstruction numbers which are shows the exact coefficient counts. It also shows the error as RMSE because min and max scaling values. These numbers describe an eight-element blood metadata vector and a four element urine metadata vector. Fig. 7 shows reconstruction of the seven-value release descriptor.

6.3 Urine release-metadata results

The urine data analysis shows 8,154 creatinine results, and 8,153 creatinine ratio results. Fig. 8 shows a metadata-vector framework.

Table 7: Original release-metadata dictionary reduction results

State	Coeff. kept	Keep (%)	RMSE	Cosine	Energy (%)
Blood	4/8	50	0.068	0.993	98.64
Blood	2/8	25	0.239	0.911	82.53
Urine	2/4	50	0.089	0.993	98.53
Urine	1/4	25	0.454	0.810	49.26

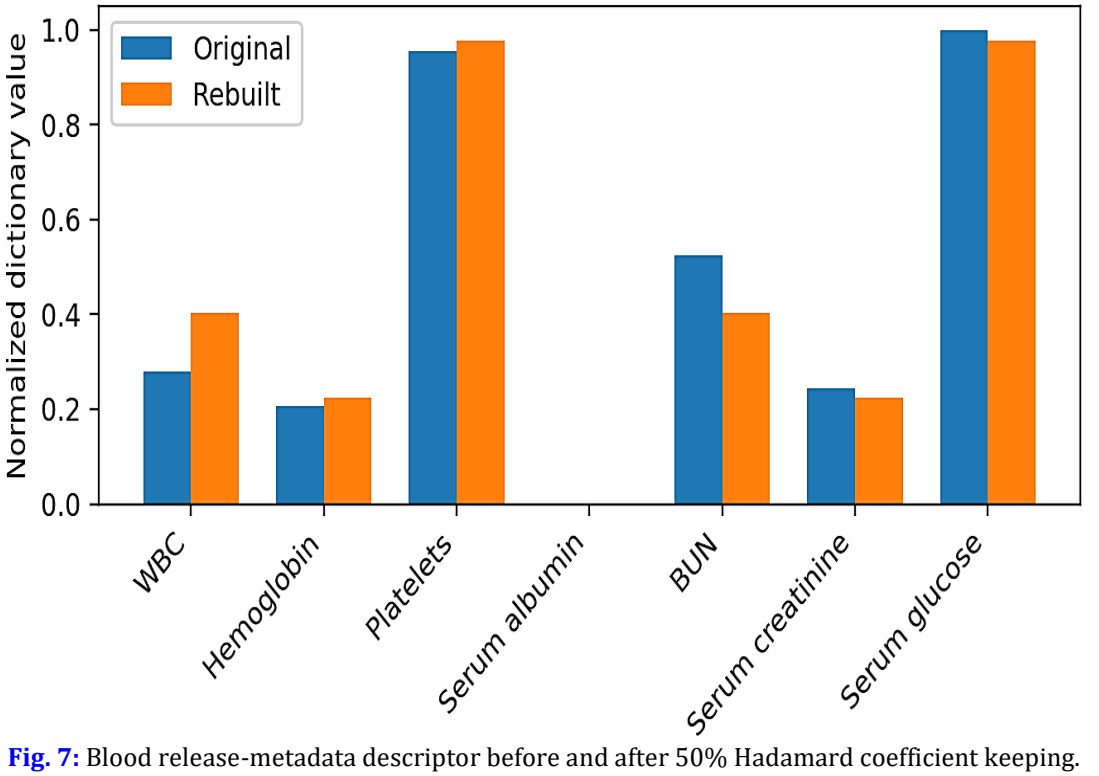


Fig. 7: Blood release-metadata descriptor before and after 50% Hadamard coefficient keeping.

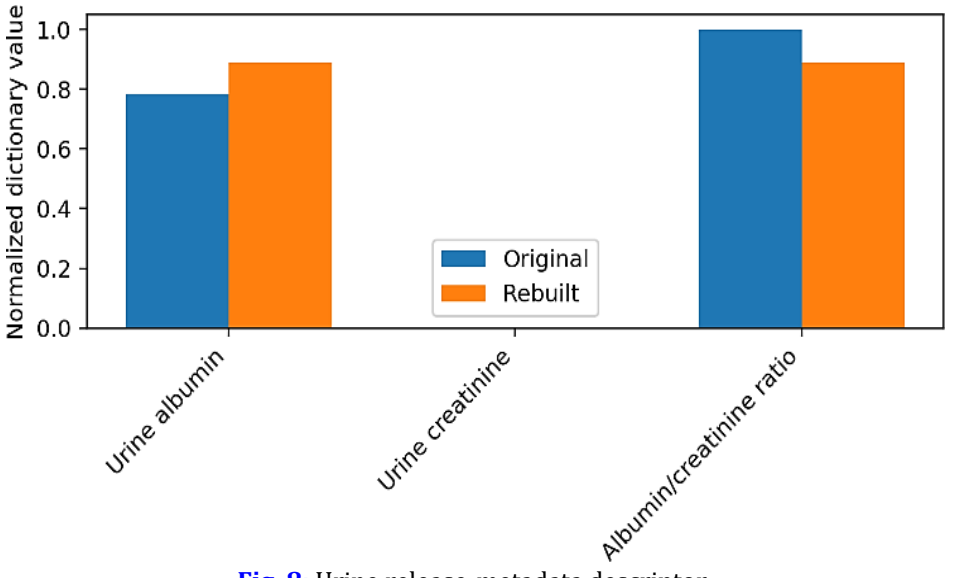


Fig. 8: Urine release-metadata descriptor.

6.4 Cross-branch coefficient concentration

Fig. 9 shows comparative outcomes of original and re-build lab data with respect to our proposed method. From the figure we see that, using quantum dictionary-based analysis produces better formations.

6.5 Answer to the research question

Our analysis shows that the answer lies at the data-structure level. A classical key–value schema can store both the retained image coefficients and the laboratory release values, and the dictionary combinations built on it ran successfully in all experiments.

6.6 Sensitivity to the number of kept states

Fig. 10 shows the original SSIM change for the two lung images. At 50% coefficient keeping, both images were above 0.97 SSIM. At 25%, both were above 0.90. At 12.5%, both were close to 0.81. Fig. 11 shows the public range widths after a log display. It is useful for seeing scale differences. It does not describe within-patient variation.

6.7 Example of one future multimodal dictionary record

A new analysis could use separate key value combinations. Image keys may start with 00, blood keys with 01, and urine keys with 10. For example,

$$S_F = \{(000001, a_1), (000010, a_2), (010001, b_1), (010010, b_2), (100001, u_1)\}. \quad (11)$$

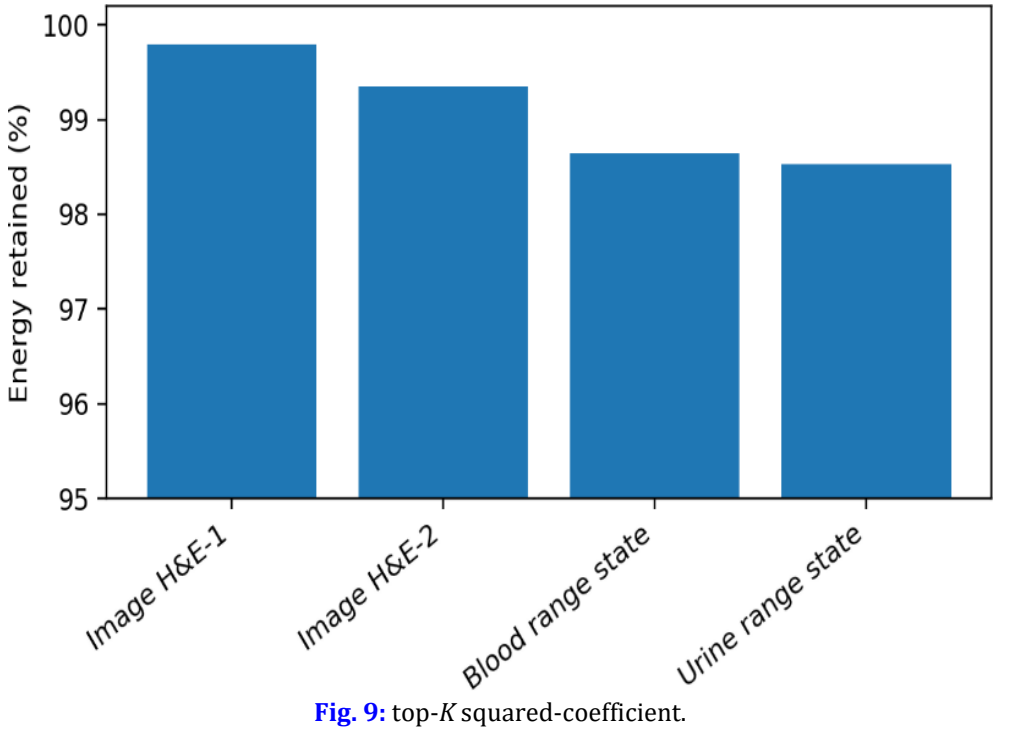


Fig. 9: top-K squared-coefficient.

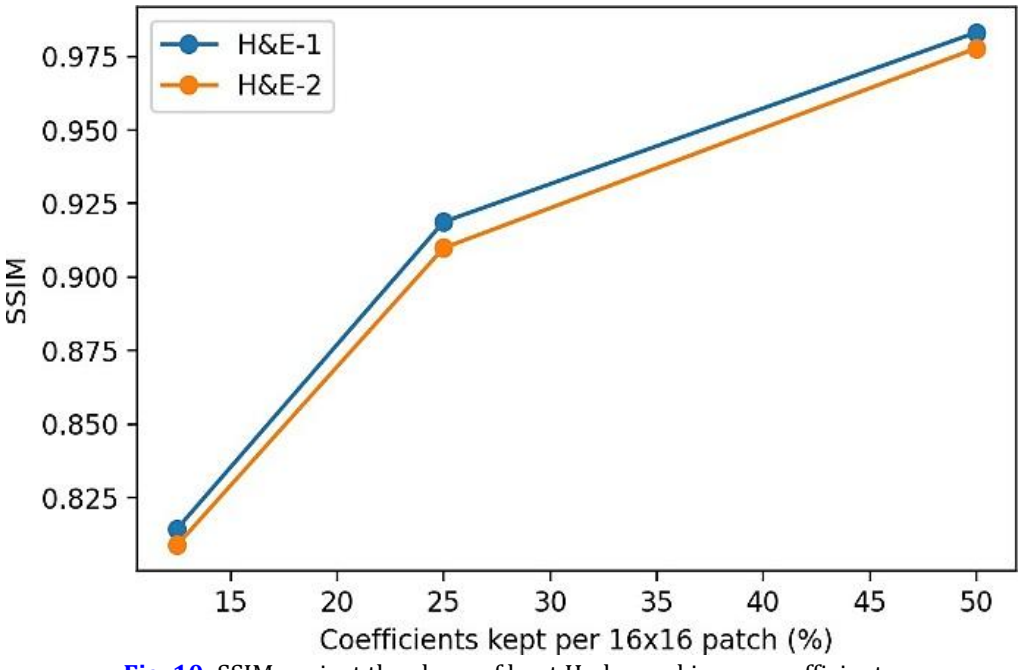


Fig. 10: SSIM against the share of kept Hadamard image coefficients.

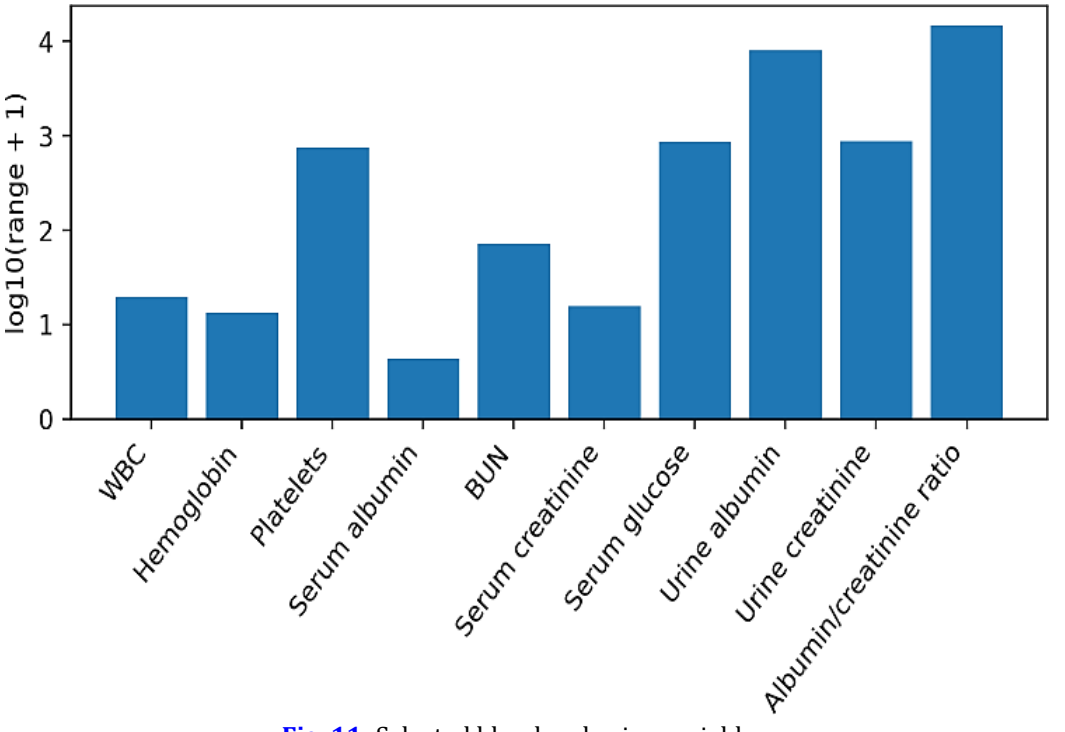


Fig. 11: Selected blood and urine variables.

Table 8: Numerical sensitivity of the 50% release-metadata descriptors

State	Variant	RLE	Cosine
Blood	Initial log range ×q	0.117	0.993
Blood	No availability weight	0.112	0.994
Blood	No log transform	0.087	0.996
Blood	Identity top-K	0.207	0.978
Urine	Initial log range ×q	0.121	0.993
Urine	No availability weight	0.121	0.993
Urine	No log transform	0.308	0.951
Urine	Identity top-K	0.000	1.000

The prefix identifies the modality. The remaining bits identify a feature. A separate mask bit or mask field can record whether a value was observed.

6.8 Quantitative descriptor sensitivity

Table 8 shows the qualitative values for validations. The outcomes indicate the metadata should not be overestimated. For urine, identity top-*K* keeping reconstructs the small padded descriptor. This indicates that the better retention number is a property of the positive vector and its padding.

7. Discussion

This analysis shows that Hadamard variations framework has useful outcomes for the two demonstration images with small values to high similarity values. On the other hand, DCT baseline provides higher PSNR and SSIM on both images. H&E-1 has 30.85 dB PSNR at 25% keeping. The high ratio of framework is providing small non-negative vectors. The image and the laboratory values show in the table are showing different values for different experiments. We basically using the similar dictionary-based analysis. Both can use a feature key, a value, an optional mask, a logged update rule, and a sparse output. It is not biological coherence. FRQI, NEQR, and QPIXL provide quantum image representations. Q-MedDict is a classical dictionary simulation inspired by gate actions.

8. Limitations

The main limitations are substantial.
1) the data about image and lab-based data are not from the same patients due to lack of patients data.
2) The lab-based data utilizes the metadata.
3) The image sources only two web-sourced examples.

9. Future work

In our next research, we will focus on demographic lung cancer data from known sources. All the experiments, lab data, and public data will be verified before going to the experiments. Moreover, we will compare with classical machine leaning outcomes with proposed quantum-based outcomes.

10. Conclusion

Our proposed method Q-MedDict is a classical quantum-based dictionary approach. It presents data with respect to bit-string keys and applies gate-like values. It is a simple method to utilize quantum concept without using quantum hardware. With this approach, we can achieve real quantum level outcomes using classical computer. We have used multiple data such DCT and PCA/KLT images. DCT outperforms the Hadamard gate on both demonstration images more than 25%. However, quantum-based dictionary model provides reliable outcomes and framework.

CRediT Author Contribution Statement

Sazia Parvin: Conceptualization, Formal analysis, Methodology, Software, Validation. **Md Sarwar Kamal:** Data curation, Visualization, Writing - Original draft, Supervision, Writing - Reviewing and editing. All authors have read and agreed to the published version of the manuscript.

Ethics Statement

This work uses public, de-identified data documentation and public web images. No new participant recruitment, intervention, or private health record access was performed.

Funding Declaration

This research did not receive any specific grant from funding agencies in the public, commercial, or not-for-profit sectors.

Data Availability Statement

Lung images data are used from the publicly available sources. The link is given bellow:
https://portal.imaging.datacommons.cancer.gov/collections/cmb_lca/.
Laboratory metadata are available from the following sources:
https://wwwn.cdc.gov/Nchs/Data/Nhanes/Public/2021/DataFiles/CBC_L.htm,
https://wwwn.cdc.gov/Nchs/Data/Nhanes/Public/2021/DataFiles/BIOPRO_L.htm and
https://wwwn.cdc.gov/Nchs/Data/Nhanes/Public/2021/DataFiles/ALB_CR_L.htm.

Conflict of Interest

The authors received no specific financial support for the research, authorship, or publication of this work.

Artificial Intelligence (AI) Use Disclosure

The authors declare that Generative AI tools were used for language editing and manuscript revision support. The authors reviewed the scientific content and checked the numerical results.

Supporting Information

Not applicable.

References

[1] M. S. Kamal, S. F. Nimmy, Quantum advantages with dictionary-based quantum data centre design for medical data, In: S. Roy Chowdhury, N. Dey, T. Guha, S. J. Fong, (eds) Proceedings of International Symposium on Innovations in Computer Vision and Applications (ISICVA

2025) Lecture Notes in Networks and Systems, Springer, Cham., 2026, 2015, doi: 10.1007/978-3-032-28206-4_2.

[2] L. Jacob, K. Thomas, L. C. Samuel, S. S. Thomas, Chapter 11 - Fusion Techniques for medical imaging and clinical data towards precision diagnostics and personalized care, Ed(s): S. Eslamian, P. Nanjundan, J. George, F. Eslamian, Multimodal Learning Using Heterogeneous Data, Morgan Kaufmann, 2026, 139-155, doi; 10.1016/B978-0-443-27528-9.00010-3.

[3] A. Siva M, C. L. Chowdhary Multi-modal personalized federated learning with adaptive differential privacy for medical image classification and a privacy-preserving approach, *Scientific Reports*, 2026, **16**, 21743, 10.1038/s41598-026-49896-z.

[4] N. Liu, G. Han, Q. Gu, Y. Zhang, M. Chen, A new era of precision diagnosis and treatment for lung cancer: Artificial intelligence-driven multimodal data integration and clinical applications, *Cell Death & Disease*, 2026, **17**, 534, doi: 10.1038/s41419-026-08769-z.

[5] F. Ahmed, N. S. Naz, S. Khan, A. U. Rehman, W. M. Ismael, M. A. Khan, Explainable artificial intelligence (xai) in medical imaging: a systematic review of techniques, applications, and challenges, *BMC Medical Imaging*, 2026, **26**, 37, doi: 10.1186/s12880-025-02118-w.

[6] R. Vavekanand, A comprehensive review of multimodal large language models for medical imaging and omics data, *Archives of Computational Methods in Engineering*, 2026, **33**, 6149–6171, doi: 10.1007/s11831-026-10504-y.

[7] M. Liu, J. Villazon, A. Forjaz, X. Tian, R. Fan, S. Wang, L. Shi, D. Wirtz, A. L. Kiemen, 3D multi-omics tumour atlases: from technology to biology and clinical translation, *Nature Reviews Cancer*, 2026, **26**, 762–789, doi: 10.1038/s41568-026-00940-0.

[8] Z. Li, Y. Li, J. Xiang, X. Wang, S. Yang, X. Zhang, F. Eweje, Y. Chen, X. Luo, Y. Li, J. Mulholland, C. Bergstrom, T. Kim, F. Maria Olguin, S. Willens, J. J. Nirschl, R. West, J. Neal, M. Diehn, R. Li , AI-enabled virtual spatial proteomics from histopathology for interpretable biomarker discovery in lung cancer, *Nature Medicine*, 2026, **32**, 231–244, 2026, doi: 10.1038/s41591-025-04060-4.

[9] K. S. Rawat, M. Yadav, Analyzing quantum computing applications across key scientific domains using trends and visual analytics, *Archives of Computational Methods in Engineering*, 2026, **33**, 401–432, doi: 10.1007/s11831-025-10312-w.

[10] A. Sar, A. Kumar, S. Roy, A. Kaushish, T. Choudhury, S. S. Alqahtani, A. Abraham, Quantum machine learning in medical image analysis: From diagnostics to surgery planning, *IEEE Access*, 2026, **14**, 27690-27732, 2026, doi: 10.1109/ACCESS.2026.3663498.

[11] P. Suyal, K. K. Gola, C. Chakraborty, R. Kanauzia, M. Suyal, Mridula, Applications of quantum-inspired soft computing for intelligent data processing in real-life scenarios-Chapter 10, in Quantum-Inspired Approaches for Intelligent Data Processing, Editor(s): B. Balusamy, S. Avdhesh Yadav, S. Ramesh, M. Vinoth Kumar, 223–257, 2026, doi: 10.1002/9781394336449.ch10.

[12] C. Daka, S. Bhattacharyya, A novel quantum convolutional neural network framework for quantum enhanced classification of pixelated colour images, *Scientific Reports*, 2026, **16**, 10828, doi: 10.1038/s41598-026-45140-w.

[13] S. Somvanshi, M. M. Islam, A. Rafe, A. G. Tusti, A. Chakraborty, A. Baitullah, T. I. Chowdhury, N. Alnawmasi, A. Dutta, S. Das, Bridging the black box: A survey on mechanistic interpretability in AI, *ACM Computing Surveys*, 2026, **58**, 1–35, doi: 10.1145/3787104.

[14] Q. Wan, C. Gao, R. Wang, X. Chen, A survey on interpretability in visual recognition, *IEEE Transactions on Pattern Analysis and Machine Intelligence*, 2026, **48**, 8547–8566, doi: 10.1109/TPAMI.2026.3672629.

[15] A. Sadeghi, F. Hajati, A. Argha, N. H. Lovell, M. Yang, H. Alinejad-Rokny, Interpretable graph-based models on multimodal biomedical data integration: A technical review and benchmarking, *Nature Communications*, 2026, **17**, 5405, doi: 10.1038/s41467-026-74126-5.

[16] A. Muneer, M. Waqas, M. B. Saad, E. Showkatian, R. Bandyopadhyay, H. Xu, W. Li, J. Y. Chang, Z. Liao, C. Haymaker, L. S. Soto, C. C. Wu, N. I. Vokes, X. Le, L. A. Byers, D. L. Gibbons, J. V. Heymach, J. Zhang, J. Wu, From classical machine learning to emerging foundation models: Review on multimodal data integration for cancer research, *Artificial Intelligence Review*, 2026, **59**, 119, doi: 10.1007/s10462-026-11522-9.

[17] X. Luo, X. Wang, F. Eweje, X. Zhang, J. L. G. Marti, S. Cascarino, S. Yang, Y. Li, R. Quinton, J. Xiang, Y. Ji, Z. Li, Y. Chen, C. Bergstrom, T. Kim, F. M. Olguin, K. Yuan, M. Abikenari, A. Heider, S. Willens, R. Li, Ensemble learning of pathology foundation models for precision oncology, *Cancer Cell*, 2026, **44**, 1981–1996, doi: 10.1016/j.ccell.2026.08.008.

[18] S. Rostami, C. Gue´rendel, M. Soliman, H. W. Stutterheim, O. Maxouri, D. I. Rodr´ıguez Sa´nchez, S. Ursprung, N. Boveradze, G. Agrotis, K. Chupetlovska, F. Castagnoli, F. Landolfi. E. K. Hong. A. D. Pizzi, N. Gennaro, M. A. Abdelatty, W. Jutidamrongphan, L. Petrychenko, P. Matkulcik, A. Salgado-Parente, F. M. Arico, S. Benson, P. Snaebjornsson, Z. Bodalal, R. G. H. Beets-Tan, Tumor morphology on ct radiomics is largely driven by the local anatomical environment, not the primary tumor type, *European Radiology Experimental*, 2026, **10**, 10.1186/s41747-026-00691-5.

[19] B. S. Sahin, M. S. Khalil, A transparent rule-based screening and personalized nutrition recommendation framework for biochemical health data: Development and validation in 46,750 NHANES adults, *Journal of Intelligent Decision Making and Information Science*, 2026, 3, 2598–2616.

[20] S. Herna´ndez-Orozco, A. Uthamacumaran, F. Herna´ndez Quiroz, K. Saeb-Parsy, H. Zenil, Integrative adaptive indexes from noisy routine haematological markers can predict and discriminate health status and biological age, *Computers in Biology and Medicine*, 2026, **208**, 11162, doi: 10.1016/j.compbiomed.2026.111628.

[21] B. Suwatronnakorn, A. Wipattanakitcharoen, T. Wuttiputhanun, A. Leelahavanichkul, N. Townamchai, Y. Avihingsanon, S. Udomkarnjananun. Reliability of spot urine protein-to-creatinine and urine albumin-to-creatinine ratios in acute kidney injury: A cohort study, *American Journal of Kidney Diseases*, 2026, doi: 10.1053/j.ajkd.2026.06.026.

[22] H. Zhang, Y. Wang, J. Wang, H. Li, Interpreting the black box: Interpretable machine learning and systems pharmacology in small-molecule therapeutics, *Pharmaceutics*, 2026, **18**, 743, doi: 10.3390/pharmaceutics18060743.

[23] J. Spronck, L. van Eekelen, D. van Midden, J. Bogaerts, L. Tessier, V. Dechering, M. Demirel-Andishmand, G. S. de Souza, R. Nemeth, E. Munari, G. Bogina, I. Girolami, A. Eccher, B. Acs, C. Boyaci, N. Klubickova, M. Looijen-Salamon, S. Vos, F. Ciompi, A tissue and cell-level annotated H&E and PD-L1 histopathology image dataset in non-small cell lung cancer, *IEEE Journal of Biomedical and Health Informatics*, 2026, 1–11, doi: 10.1109/JBHI.2026.3685529.

[24] J. Monkman, A. Kilgallon, C. Lawler, R. Tubelleza, T. N. Aung, J. H. Warrell, I. Vathiotis, I. P. Trontzas, N. Gavrielatou, N. N. N. Chan, R. Czertok, S. Bookstein, K. O'Byrne, E. Markovits, D. L. Rimm, A. Kulasinghe, Metabolic characterization of tumor-immune interactions by multiplexed immunofluorescence reveals spatial mechanisms of immunotherapy response in non-small cell lung carcinoma (NSCLC), *Nature Communications*, 2026, **17**, 837, doi: 10.1038/s41467-026-68633-8.

[25] X. Liu, Y. Liu, W. Duan, J. Weng, H. Dai, F. Liu, L. Wang, M. Qian, B. Zhu, S. Wu, Y. Ye, M. Yuan, S. Hong, M. Wang, Y. Cheng, T. Chen, D. Wu, Y. Song, X. Wang, Single- cell identifies and validates human circulating Treg subtype/state Tregfci in non-small cell lung cancer, *Signal Transduction and Targeted Therapy*, 2026, **11**, 211, 2026, doi: 10.1038/s41392-026-02677-6.

[26] M. Campisi, T. Osaki, I. Dryg, C. Stornante, J. Wolff, J. Weirather, N. Weaver, M. Tarannum, I. Gillanders, A. Bers, E. Bobilev, M. S. Lineberry, P. Schol, M. Chen, K. Ota, S. R. Park, C. G. Fahey, T. C. Thai, Y. Li, Z. Li, Z-H. Li, S. Shelton, S. Hirose, C. Padrick, E, Ivanova, M. Ha, S. Yang, H. Olszewski, S. Kivlehan, P. Lizotte, K. Hagen, I. Gjeci, W. Haller, L. M. Zasadil, T. El Zarif, J. E. Berchuck, E. H. Knelson, E. J. Brea, I. Odintsov, T. Liu, V. Chiono, B. Tuladhar, , K. Ngo, E. Rosentrater, J. Raizer, N. Lineberry, M. Sur, K. Pfaff, M. Freedman, F. S. Hodi, M. Y. Tolstorukov, M. G. Oser, M. Sheffer, C. S. Mitsiades, M. J. Barnes, V. A. Appleman, P. C. Gokhale, R. D. Kamm, C. P. Paweletz, R. Romee, S. Rodig, D. A. Barbie, N. R. Mahadevan, Vascular STING activation facilitates NK cell anti-tumor immunity in small cell lung cancer, *Cancer Cell*, 2026, 44, 858–878.e16, doi: 10.1016/j.ccell.2026.02.008.

[27] Q. Li, S. Zhang, J. Jiang, H. Li, Z. Li, J. Zhu, J. Tong, F. Wu, Research frontiers and emerging trends in sex and gender differences in chronic obstructive pulmonary disease: A bibliometric analysis, *Journal of Thoracic Disease*, 2026, doi: 10.21037/jtd-2025-1988.

[28] N. A. Alwan, N. M. Al-Saidi, S. J. Obaiys, N. F. B. M. Noor, M. Ahmad, A comprehensive review on classification of quantum image representations, *Archives of Computational Methods in Engineering*, 2026, **33**, 3123–3181, doi: 10.1007/s11831-025-10369-7.

[29] T. S. Atia, Z. A. Ali, A. Y. Yousuf, Soft-quantum computing integration: automated design and optimization of scrambling circuits for NEQR and GNEQR image using GAs and fuzzy logic, *Quantum Information Processing*, **25**, 246, doi: 10.1007/s11128-026-05256-4.

[30] N. Vinayak, S. Ahmad, Qxrnet: a hybrid CNN–QNN model with resolution-conditioned feature

extraction and variational quantum circuit, *Quantum Machine Intelligence*, 2026, **8**, 2026, doi: 10.1007/s42484-026-00377-6.
[31] A. H. Salehi Shayegan, Quantum image processing filters based on FRQI representation, *Quantum Information Processing*, 2026, **25**, 293, doi: 10.1007/s11128-026-05321-y.
[32] N. Tarek, An optimal hybrid quantum-classical representation for robust photonic image processing on NISQ devices, *Quantum Information Processing*, 2026, **25**, 295, doi: 10.1007/s11128-026-05314-x.
[33] A. Xu, B. Sun, Z. Wang, S.-M. Fei, Separability criteria via type-ii discrete cosine transform, *Advanced Quantum Technologies*, 2026, 9, e70453, doi: 10.1002/qute.70453.

Publisher Note: The views, statements, and data in all publications solely belong to the authors and contributors. G R Scholastic is not responsible for any injury resulting from the ideas, methods, or products mentioned. G R Scholastic remains neutral regarding jurisdictional claims in published maps and institutional affiliations.